University of California Santa Barbara

# High-Power Broadband Multispectral Source on a Hybrid Silicon Chip

John E. Bowers, Eric J. Stanton, and Alexander Spott

Department of Electrical and Computer Engineering

March 14, 2017

# REPORT DOCUMENTATION PAGE

The public reporting burden for this collection of information is estimated to average 1 hour per response, including the time for reviewing instructions, searching existing data sources, gathering and maintaining the data needed, and completing and reviewing the collection of information. Send comments regarding this burden estimate or any other aspect of this collection of information, including suggestions for reducing the burden, to the Department of Defense, Executive Service Directorate (0704-0188). Respondents should be aware that notwithstanding any other provision of law, no person shall be subject to any penalty for failing to comply with a collection of information if it does not display a currently valid OMB control number.
**PLEASE DO NOT RETURN YOUR FORM TO THE ABOVE ORGANIZATION.**

| 1. REPORT DATE *(DD-MM-YYYY)* | 2. REPORT TYPE | 3. DATES COVERED *(From - To)* |
|---|---|---|
| 14-03-2017 | Final Technical Report | 28-08-2013 - 31-12-2016 |

| 4. TITLE AND SUBTITLE | 5a. CONTRACT NUMBER |
|---|---|
| High-Power Broadband Multispectral Source on a Hybrid Silicon Chip | N00014-13-C0147 |

**5b. GRANT NUMBER**

**5c. PROGRAM ELEMENT NUMBER**

| 6. AUTHOR(S) | 5d. PROJECT NUMBER |
|---|---|
| John Bowers, Alex Spott, and Eric Stanton | |

**5e. TASK NUMBER**

**5f. WORK UNIT NUMBER**

| 7. PERFORMING ORGANIZATION NAME(S) AND ADDRESS(ES) | 8. PERFORMING ORGANIZATION REPORT NUMBER |
|---|---|
| University of California, Santa Barbara<br>Office of Research, 3227 Cheadle Hall<br>Santa Barbara, CA 93106-2050 | |

| 9. SPONSORING/MONITORING AGENCY NAME(S) AND ADDRESS(ES) | 10. SPONSOR/MONITOR'S ACRONYM(S) |
|---|---|
| Office of Naval Research<br>875 N. Randolph St.<br>Arlington, VA 22203 | ONR |
| | 11. SPONSOR/MONITOR'S REPORT NUMBER(S) |

**12. DISTRIBUTION/AVAILABILITY STATEMENT**
Distribution A - Approved for public release; distribution is unlimited.

**13. SUPPLEMENTARY NOTES**

**14. ABSTRACT**
Successful demonstrations of integrated lasers and beam combiners spanning the near-infrared (NIR) to the midwave-infrared (MWIR) are presented. Multi-spectral lasers integrated on Si are shown and various waveguide materials suitable for wavelengths from the ultra-violet (UV) to the longwave-infrared (LWIR) are discussed. Recent work integrating 2.0-$\mu$m diode and 4.8-$\mu$m quantum cascade lasers (QCLs) on Si extend the previously demonstrated 1.0-$\mu$m, 1.3-$\mu$m, and 1.5-$\mu$m diode lasers on Si to the MWIR. Distributed feedback (DFB) QCLs integrated on the silicon-on-nitride-on-insulator (SONOI) waveguide platform are demonstrated and emit over 200 mW pulsed output power at room temperature. Improvements are made to the 1.5-$\mu$m diode lasers to increase output power and brightness. Spectral beam combining elements with low loss for the visible (VIS) to the shortwave-infrared (SWIR) are demonstrated and devices are fabricated (measurements in progress) in the MWIR. We detail the results of this project including the motivations, applications, and project outcomes. We summarize insights and projections of the output power and spectral bandwidth that we expect are feasible to demonstrate with further research.

**15. SUBJECT TERMS**
Photonic integrated circuits, distributed feedback lasers, MWIR, LWIR QCLs, beam combining.

| 16. SECURITY CLASSIFICATION OF: | | | 17. LIMITATION OF ABSTRACT | 18. NUMBER OF PAGES | 19a. NAME OF RESPONSIBLE PERSON |
|---|---|---|---|---|---|
| a. REPORT | b. ABSTRACT | c. THIS PAGE | | | John Bowers |
| U | U | U | UU | 25 | 19b. TELEPHONE NUMBER *(Include area code)*<br>805-893-8447 |

**Abstract**

Successful demonstrations of integrated lasers and beam combiners spanning the near-infrared (NIR) to the midwave-infrared (MWIR) are presented. Multi-spectral lasers integrated on Si are shown and various waveguide materials suitable for wavelengths from the ultra-violet (UV) to the longwave-infrared (LWIR) are discussed. Recent work integrating 2.0-µm diode and 4.8-µm quantum cascade lasers (QCLs) on Si extend the previously demonstrated 1.0-µm, 1.3-µm, and 1.5-µm diode lasers on Si to the MWIR. Distributed feedback (DFB) QCLs integrated on the silicon-on-nitride-on-insulator (SONOI) waveguide platform are demonstrated and emit over 200 mW pulsed output power at room temperature. Improvements are made to the 1.5-µm diode lasers to increase output power and brightness. Spectral beam combining elements with low loss for the visible (VIS) to the shortwave-infrared (SWIR) are demonstrated and devices are fabricated (measurements in progress) in the MWIR. We detail the results of this project including the motivations, applications, and project outcomes. We summarize insights and projections of the output power and spectral bandwidth that we expect are feasible to demonstrate with further research.

**Table of Contents**

## 1. Introduction

For applications in manufacturing, remote sensing, medicine, military, and fundamental science, an ideal laser would have high output power and a diffraction-limited beam. The figure-of-merit to describe this property is the brightness, which scales proportional to output power and inverse to the beam quality factor $M^2$. Lasers that are both compact and have high-brightness are challenging to realize. As the size of the laser is reduced, either the output power is decreased or the $M^2$ is increased, primarily due to a combination of thermal effects and high optical intensities [1,2]. Many applications, such as spectroscopy, infrared countermeasures, free-space communication, and industrial manufacturing, can benefit from a light source emitting at multiple frequencies. A compact and high-brightness laser can then be achieved by spectral beam combining [3]. This photonic integrated circuit (PIC) may expand the spectral bandwidth of currently available optical sources at lower cost, smaller size, reduced vibration sensitivity, and higher brightness.

### 1.1. Background and Motivation

Over the past decade, advances in heterogeneous lasers on silicon (Si) enable such a multi-frequency and high-brightness laser to be integrated on a single cost-effective substrate [4,5]. With multiple die bonding [6,7] materials exhibiting optical gain at various wavelengths are brought together onto a Si chip and lasers are formed with integrated mirrors. Outputs from each laser can be combined with various stages of wavelength division multiplexing optical elements [8], as shown in Fig. 1. Semiconductor optical amplifiers (SOAs) are critical components for many kinds of photonic integrated circuits to increase output power or maintain signal levels as the signal propagates throughout a large number of optical components [9]. In our approach, SOAs are integrated on the same platform with the lasers on Si and, in addition to the concept of Fig. 1, could be used to increase power following each intra-band combiner.
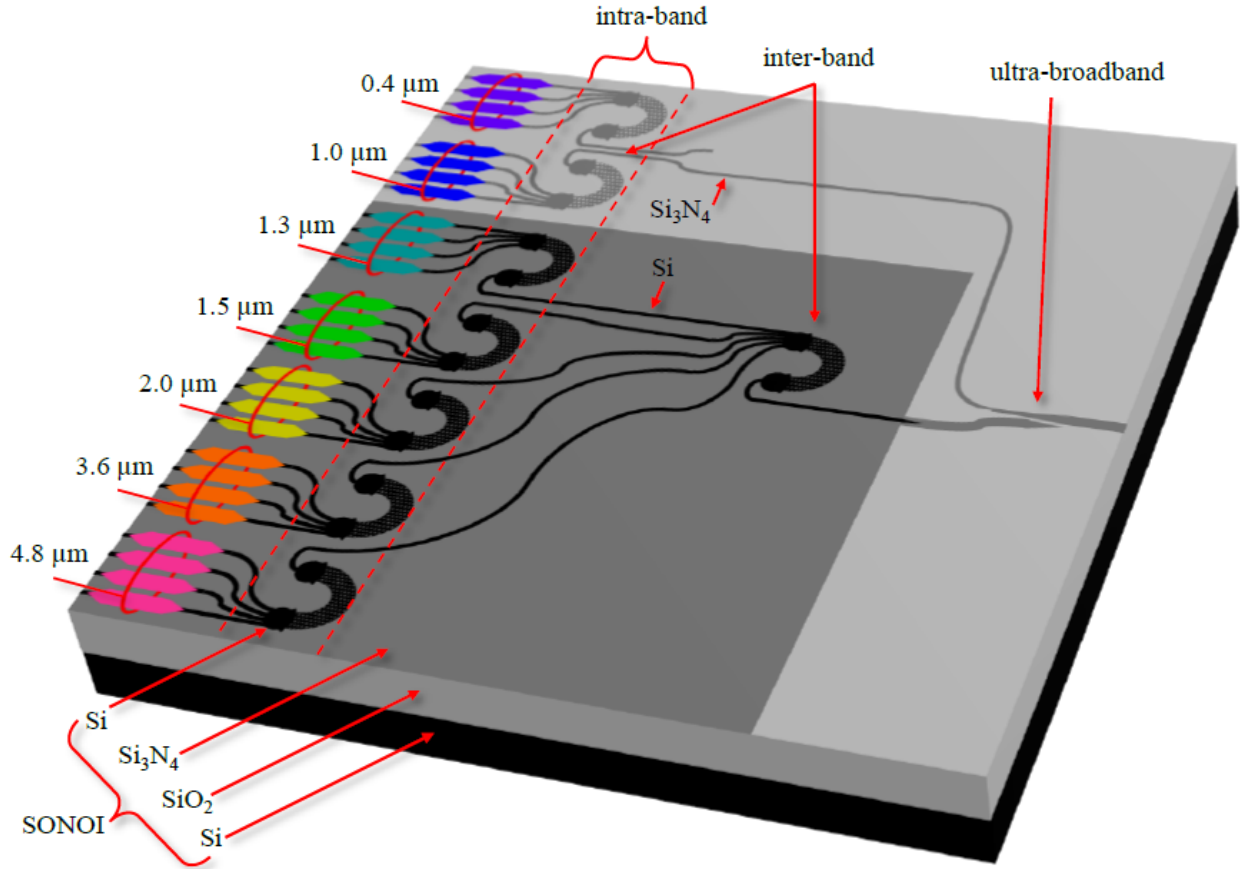
Figure 1. Schematic diagram of a multi-spectral laser on a Si substrate with the SONOI waveguide platform.

## 1.2. Objectives

This manuscript reviews recent progress on integration of multiple laser sources on a chip that combines the outputs to a single waveguide. Each laser gain material could support many lasers with densely spaced wavelengths, similar to modern optical communication systems spanning the optical bandwidth of the erbium-doped-fiber-amplifier with densely-spaced frequency channels. To extend the spectral capacity of the Si-on-insulator (SOI) platform beyond the transmission window supported by a Si-core and silicon dioxide ($SiO_2$)-clad waveguide, a silicon nitride ($Si_3N_4$) waveguide layer can be added in between the Si and silicon dioxide layers [8]. Optical sources at 1.0-µm [18], 1.3-µm [10], 1.5-µm [4], 2.0-µm [11], and 4.8-µm [12] wavelengths on Si have been demonstrated separately on either the SOI or SONOI platforms.

Efficient integrated spectral combining elements were investigated for coarse and dense wavelength combining stages. In particular, we reduced the losses associated with the arrayed waveguide gratings (AWGs) used in the dense wavelength combining stage. The following sections present the architecture for this multi-frequency high-brightness laser, discuss materials for broadband and low-loss operation, review demonstrations of lasers on Si emitting at different wavelengths, and present integrated wavelength combining devices compatible with these lasers on Si.

## 2. Approach

An ultra-broadband multi-spectral laser on Si is can be constructed by employing existing heterogeneous integration technology and building lasers on Si by direct wafer bonding [13,14]. This fully integrated device is schematized in Fig. 1, showing presently demonstrated spectral bands of lasers on Si operating at 1.3-µm [6,10], 1.5-µm [4,9], 2.0-µm [11,15], and 4.8-µm [12,16] wavelengths, based on indium phosphide (InP). Active devices have also been integrated with $Si_3N_4$ at 1.0-µm (based on gallium arsenide (GaAs)) [18] and 1.5-µm [17]. The spectral bands at 0.4-µm and 3.6-µm wavelengths can be realized with gallium nitride (GaN) and gallium antimonide (GaSb) based materials, respectively.

Spectral beam combining of each laser wavelength to a single output waveguide is achieved in several stages from dense to coarse wavelength division multiplexing (WDM). There is no inherent loss to combining different wavelengths, unlike combining identical lasers, which has inherent 1/N combiner loss. Note that AWGs efficiently combine light from more than two channels both for the dense WDM and for the coarse WDM. Adiabatic couplers can be designed to combine light for coarse WDM with just two inputs. Lasers with wavelengths longer than ~1.1 µm are integrated on Si waveguides, while shorter wavelength lasers are on $Si_3N_4$ waveguides. The final ultra-broadband combining stage has been demonstrated [8] to combine light from the visible (0.76 µm) to the mid-infrared (3.6 µm) with high fundamental mode transmission. Furthermore, simulations show efficient operation in the range of 0.35–6.7 µm, however, this was not verified due to limited availability of optical sources. To obtain high brightness, every element of this PIC must be efficient. For the lasers, high wall-plug efficiency and output power are critical figures-of-merit. SOAs may also be included to boost the power of each spectral band. The beam combining elements must have low on-chip loss and transmit light to the fundamental modes of each wavelength in a single output waveguide.

The brightness ($B$) is defined by the output power ($P$) and the beam quality factor ($M^2$) as: $B = P/M^2$. The transverse divergence angles ($\theta_\perp$ and $\theta_\parallel$) can be expressed from the diffraction-limited divergence angles ($\theta_{\perp,0}$ and $\theta_{\parallel,0}$) modified by the beam quality factors ($M_\perp^2$ and $M_\parallel^2$): $\theta_\perp = \theta_{\perp,0} M_\perp^2$ and $\theta_\parallel = \theta_{\parallel,0} M_\parallel^2$. Both angles can be combined as: $M^2 = (M_\perp^4 + M_\parallel^4)^{1/2}$. The ideal condition of $M^2 = 1.0$ is achieved by tailoring the output optical mode of the laser to have an exactly Gaussian-shaped intensity profile in the vertical and the horizontal orientations. For this reason, the passive beam-combining elements must transmit a high percentage of input light to the output fundamental mode. Additionally, the output waveguide must be able to support Gaussian-shaped modes throughout the bandwidth of the multi-spectral optical sources.

## 3. Realization

Here we discuss the material platform for this photonic integrated circuit and present the demonstrations of lasers and beam combining elements that will constitute the multispectral source. The following sub-sections on the lasers and combiners are organized by wavelength.

### 3.1. Waveguide material platform

An investigation of waveguides for low-loss mid-infrared transmission has shown that Si can guide light from the near-infrared ($\sim$1.1-µm) to the mid-infrared ($\sim$7.0-µm) with low absorption loss [19,20]. $SiO_2$ and $Si_3N_4$ are commonly integrated on Si and can be layered with Si to create multiple waveguide cores and claddings in the same platform. These materials have transmission windows in the wavelength ranges of $\sim$0.35–3.5-µm and $\sim$0.35–6.7-µm, respectively [19,20], as shown in Fig. 2 (b).

We have constructed a waveguide platform with layers of Si, $Si_3N_4$, and $SiO_2$ on a Si substrate, termed Si-on-nitride-on-insulator (SONOI) [8,12,16] and depicted in Fig. 2(a). By defining waveguides in the top Si layer and depositing an upper cladding of $Si_3N_4$, light from $\sim$1.1-µm to $\sim$6.7-µm wavelengths is efficiently guided. In other areas of the same chip, the top Si layer is removed and waveguides with $Si_3N_4$ core and $SiO_2$ cladding are defined to support $\sim$0.4-µm to $\sim$3.5-µm wavelengths. For longer wavelengths in the mid-infrared, $Si_{1-x}Ge_x$ waveguides can transmit light with low-loss from 1.9-µm, to 16.7-µm [19,21,22]. This can potentially be integrated with the SONOI platform by adding the $Si_{1-x}Ge_x$ on top of the Si waveguide layer.
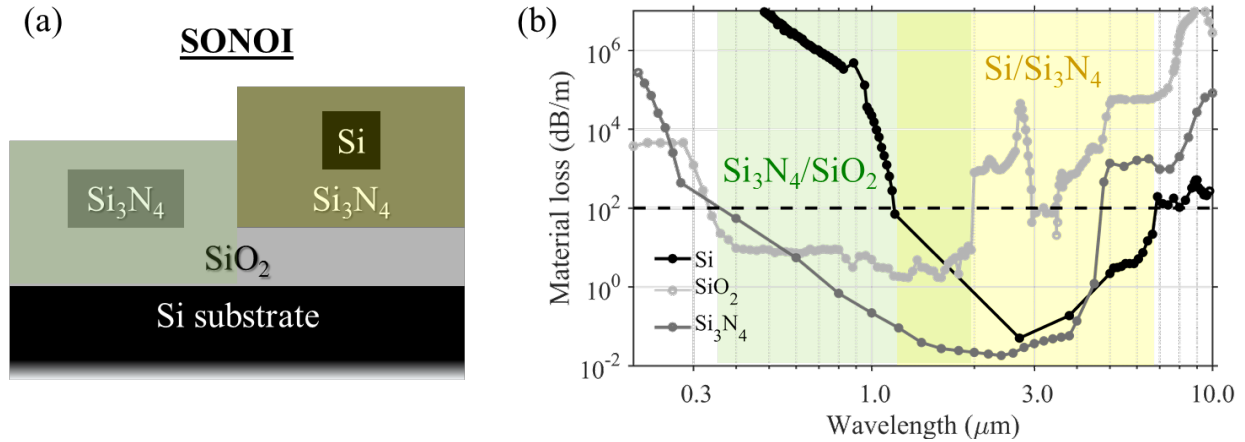


Figure 2. (a) Cross-section schematic of a SONOI waveguide co-integrated with a NOI waveguide. (b) Optical absorption loss for the materials in the SONOI platform [19].

### 3.2. Lasers heterogeneously integrated on silicon

In this section, the current spectral capabilities of heterogeneous lasers on Si are motivated and discussed. Fabrication for lasers and amplifiers at each spectral band follows a similar process, schematized in Fig. 3. More detailed processing information can be found in a recent manuscript about distributed feedback (DFB) lasers on Si [23]. Laser performance is reviewed at each wavelength and compared by the threshold currents, maximum output powers, and temperature dependencies.

a) Waveguide etching   b) Gain-material bonding   c) Gain-material etching

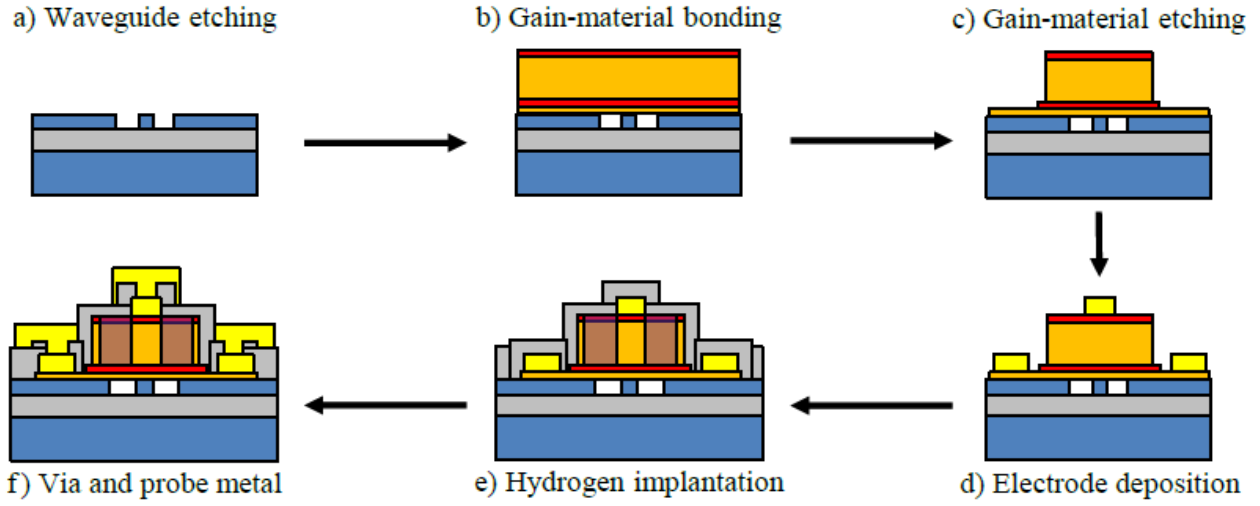f) Via and probe metal   e) Hydrogen implantation   d) Electrode deposition

Figure 3. Fabrication steps (a–e) generalized for heterogeneously integrated lasers on Si, applicable to each spectral band discussed in Section 4. For some spectral bands (*i.e.* 4.8-µm), step (e) is skipped.

### 3.2.1. Lasers at 1.0-µm on Si

Previous work on heterogeneously integrated lasers on Si substrates all use a silicon waveguide below the active region. For the demonstration of a 1.0-µm laser on Si, a $Si_3N_4$ waveguide must be used instead due to the high band-to-band optical absorption of Si at this wavelength. This waveguide is compatible with the SONOI platform, as shown in Fig. 2(a), and record low on-chip losses have been demonstrated with this waveguide. A gallium arsenide-based (GaAs) active structure is bonded on top of the $Si_3N_4$ waveguide and an upper cladding of $SiO_2$ is deposited. The first results, shown in Fig. 4(a), demonstrate pulsed output power >10 mW and other devices with threshold currents less than 20 mA for 600-µm long lasers. A cross-sectional schematic of this device is presented in Fig. 4(b). Greater output power is expected for longer lasers and further improvements can be realized by reducing the internal losses, currently measured as $\alpha_i = 6.2$ cm$^{-1}$. Current confinement in the active region is created with an AlGaAs oxidation which increased loss at the hybrid III-V/$Si_3N_4$ to $Si_3N_4$ waveguide interface. Further process development or a new current confinement strategy is expected to improve the performance.
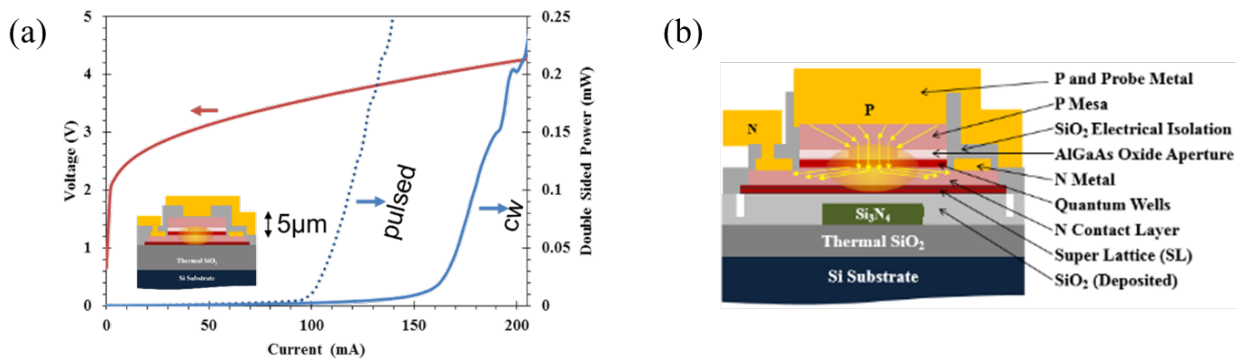


Figure 4. (a) Light output and voltage versus input current plotted for 1.0-µm laser on Si. (b) Cross-section schematic of the laser.

### 3.2.2. Lasers at 1.31-μm on Si

One of the early demonstrations of the heterogeneously integrated laser operates at 1.31-μm wavelength with an InP-based gain material [11]. A maximum output power of 32 mW is reported with a 35-mA threshold current at room temperature. Continuous-wave (CW) lasing up to 105 °C is observed. More recently, improved performance is shown with an 18-mA threshold current, 35-mW CW output power, and a wall-plug efficiency of 14 % [24]. The gain region length is only 700 μm and higher output power is expected for a design with a longer gain region. Simultaneous operation of 16 lasers arrayed on the same chip is demonstrated. This spectral band has the most mature technology for fabrication and packaging [25]. Also, 1.31-μm lasers are typically more efficient that 1.55-μm lasers, because of lower intervalence band absorption [26] and reduced Auger recombination [27].

### 3.2.3. Lasers and SOAs at 1.55-μm on Si

Since the first electrically pumped laser on Si was demonstrated [4], there has been significant focus and development to improve performance and advance this technology for large scale integration to drive down the cost of optical communication systems. The most complex PICs using heterogeneous integration are at this wavelength [7]. A recent demonstration at 1.55-μm details design optimization and performance for SOAs and lasers [9]. This work exemplifies a unique property of the heterogeneously integrated lasers and SOAs: the optical confinement is controlled lithographically by the Si waveguide width, independent of the current injection width or active region alterations. As a result, SOAs fabricated on the same chip may be designed with different values of gain and output saturation power. On-chip gain is demonstrated in the range 11–26 dB, as shown in Fig. 5(a), controlled by the Si waveguide width and corresponding to input saturation powers as high as 4 dBm. Operation over a wide bandwidth, plotted in Fig. 5(b), shows how a single SOA can amplify multi-spectral light following the intra-band combiner stage in Fig. 1.
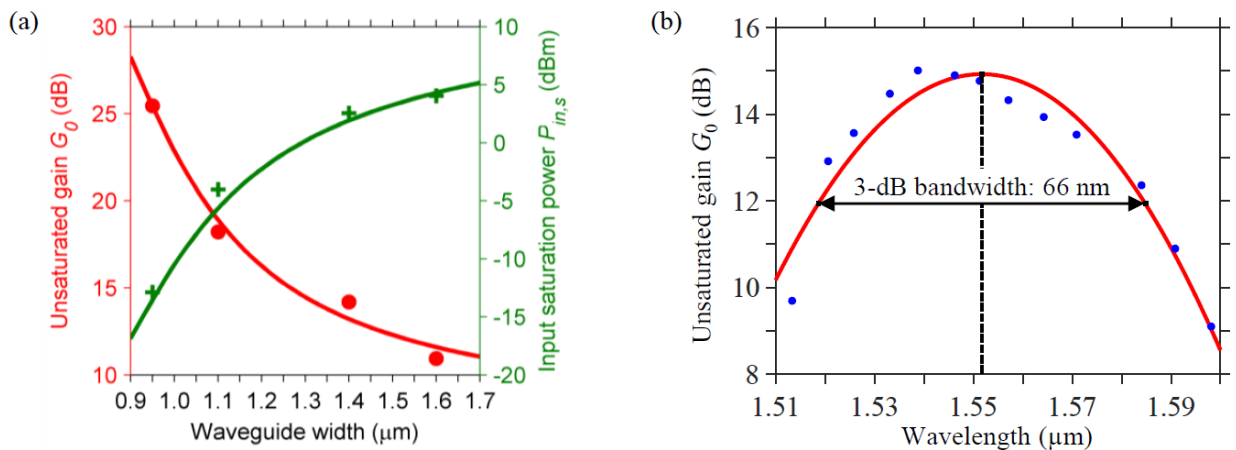


Figure 5. (a) Gain in the small-signal regime and input saturation power of an SOA operating at 1.55-μm wavelength. (b) Gain extracted as a function of the wavelength. The fit (in red) shows the 3-dB bandwidth of the device.

Prior to the application of the anti-reflective (AR) coating to the SOAs, the devices lase from the Si-waveguide facet reflections, as schematized in Fig. 6(a). Output power is measured up to 42 mW, shown in Fig. 6(b). The thermal impedance is 11 K/W [9], which is comparable to similar diodes on InP. Due to the high thermal conductivity of Si (1.56 W·cm$^{-1}$·K$^{-1}$) [28], lateral heat spreading in the Si waveguide layer is responsible for this low thermal impedance. By defining a wide mesa of 26 μm, the III–V is in contact with ~10 μm of the Si on both sides of the Si waveguide trench. Heat generated in the active region then has a low impedance path to this Si layer. Again, higher power is expected for longer gain region lengths.
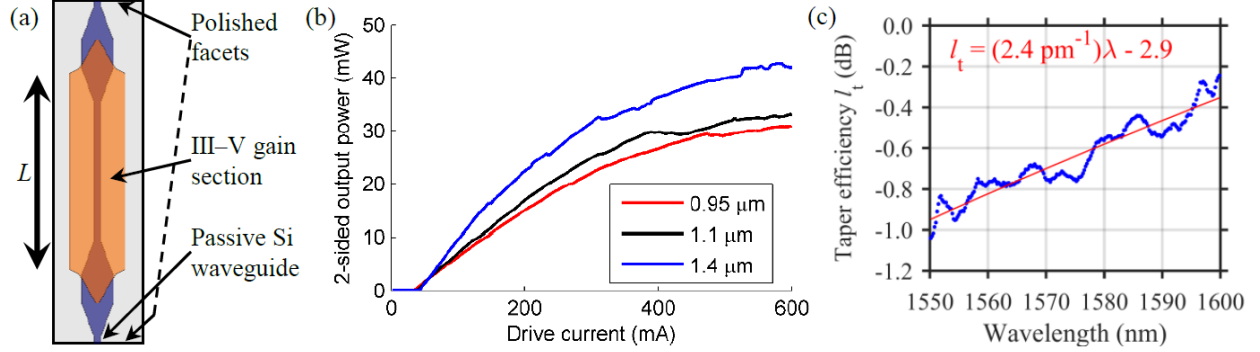


Figure 6. (a) Top-view schematic and (b) output power of a 1.55-μm laser. The polished Si-waveguide facets have a power reflection coefficient R = 0.28 for each and define the laser cavity, which includes a gain section of length L = 2 mm. (c) Extracted taper efficiency $l_t$ versus the wavelength.

A common challenge of heterogeneously integrated lasers is to produce an efficient optical mode converter between the gain and the passive waveguide regions. This taper efficiency ($l_t$), plotted in Fig. 6(c), has a maximum value of −0.25 dB and increases as the wavelength increases. It is extracted from two similar lasers with different gain ($g_1$ and $g_2$), different gain-region lengths $L_1$ and $L_2$, and a passive waveguide loss ($\alpha_{Si} \approx 50$ dB/m) as:

$$l_t = \frac{L_1 g_2 - L_2 g_1}{2(L_2 - L_1)} - \alpha_{Si} L_2. \tag{1}$$

Note that this relation depends on the wavelength and the current density. By accurately characterizing the taper loss, designs can be optimized for lasers at each wavelength for the multi-spectral laser.

### 3.2.4.  Lasers and SOAs at 2.0-μm on Si

Si exhibits both a low two-photon absorption coefficient and a high Kerr coefficient at ~2.0-μm wavelength [29]. Therefore, low waveguide propagation loss is expected in this spectral band. Also, Si provides a power-efficient platform for chip-level applications in non-linear optics [30–32], including comb generation and on-chip doubling [33], so PICs with integrated 2.0-μm active devices are highly desired.

Recently, the first laser operating at 2-μm wavelength on Si was demonstrated [12]. The first ever reported 2-μm SOA was also demonstrated on Si [16]. These devices consist of GaInAs quantum wells (QWs) bonded on top of a Si waveguide. A cross-section schematic is drawn in Fig. 7(a). The hybrid optical mode is laterally confined by the Si waveguide, while a portion of the mode overlaps the active region. The III-V mesa is terminated on both sides by a lateral taper, causing the hybrid active mode to couple into a passive Si waveguide mode. A Fabry-

Perot cavity is then formed by the polished Si facets for the lasers, and they are AR coated to form the SOAs. The laser output power, plotted in Fig. 7(b), has emission up to 4.2 mW from a single facet with a ~122-mA threshold current. CW lasing is observed up to 35 °C. The SOA on-chip gain has current and wavelength dependencies as plotted in Fig. 8. A maximum gain of 13-dB is observed and gain is demonstrated up to 50 °C.
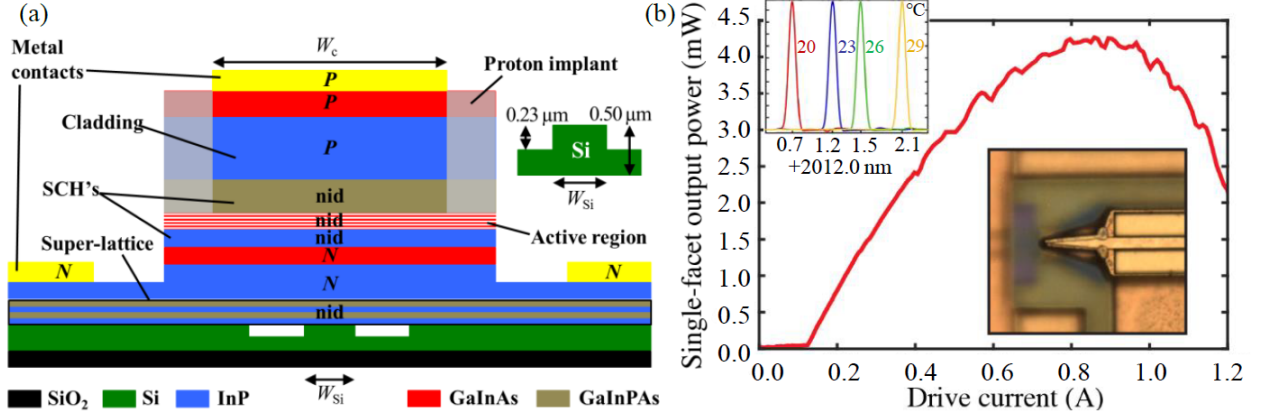


Figure 7. (a) Cross-section schematic of 2.0-μm laser or SOA on Si. (b) Output power characteristic with insets showing the laser spectra at different temperatures and a micrograph of the taper transition between the gain and passive regions.
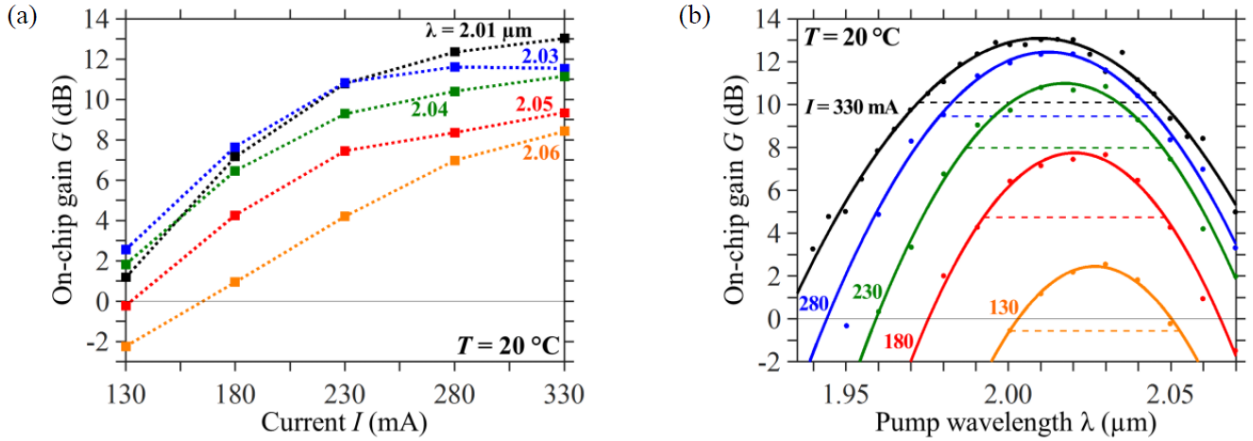


Figure 8. (a) Schematic of taper loss test structures. (b) Extracted taper loss $l_t$ wavelength dependence.

### 3.2.5. Lasers at 4.8-μm on Si

Light of longer wavelengths than 3 μm can be exploited for numerous sensing and detection applications. Chemical bond spectroscopy [34], environmental monitoring, and remote sensing [35] can potentially be addressed on an integrated Si platform. Low-cost, versatile, and complex technologies can be enabled by integrating multiple sensors on one Si chip. However, room-temperature InP-based type-I diode lasers have only been reported up to ~2.4 μm [36]. Alternatively, GaSb-based interband cascade lasers (ICL) and InP-based quantum cascade lasers (QCL) are promising candidates for extending heterogeneous integration to wavelengths

throughout the mid-infrared (3.0–8.0 µm). QCLs operate from 3.0 µm to the terahertz regime and can emit watts of CW output power [37,38].

We recently reported the first successful demonstration of QCLs on silicon [13]. The initial 4 mm-long Fabry-Perot lasers operated in pulsed mode at room temperature, and emitted up to 31 mW at $\lambda = 4.8$ µm. Figure 9(a) shows the light intensity *vs.* drive current of an integrated QCL. These devices were integrated on the SONOI platform, which consists of 1.5 µm-tall, fully etched silicon waveguides above a 400 nm-thick silicon nitride layer, a 3 µm-thick silicon dioxide layer, and a silicon substrate. These SONOI waveguides support transmission from ~1.2 to 6.7 µm [19], and can be extended to much shorter wavelengths by removing the top silicon layer and constructing SiN-on-SiO$_2$ waveguides that transmit from ~0.35 to 3.5 µm. Figure 9(b) shows an electron microscope image of a cleaved SONOI waveguide facet.
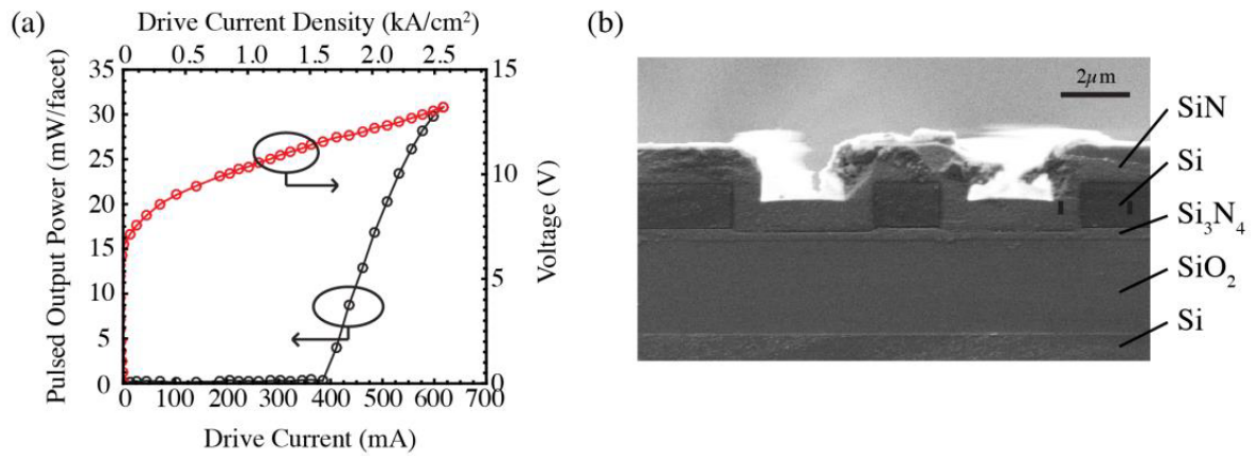


Figure 9. (a) Pulsed output power *vs.* drive current for a Fabry-Perot quantum cascade laser integrated with silicon waveguides. (b) Electron microscope image of a polished SONOI end-facet.

Figure 10(a) shows an optical microscope image of DFB QCLs heterogeneously integrated with SONOI waveguides [16]. Lasers with four different active region waveguide geometries were fabricated. Figure 10(b) shows a cross sectional schematic of each design. Designs A-C exhibit fully-etched narrow III-V ridges as in [13], with mesa widths of 4 µm, 6 µm and 8 µm, respectively. Design D has a 24 µm-wide active region with a 6 µm-wide upper InP cladding. The silicon waveguides are 1.5 µm-wide for Designs A, B, and D, and 3.5 µm for Design C.
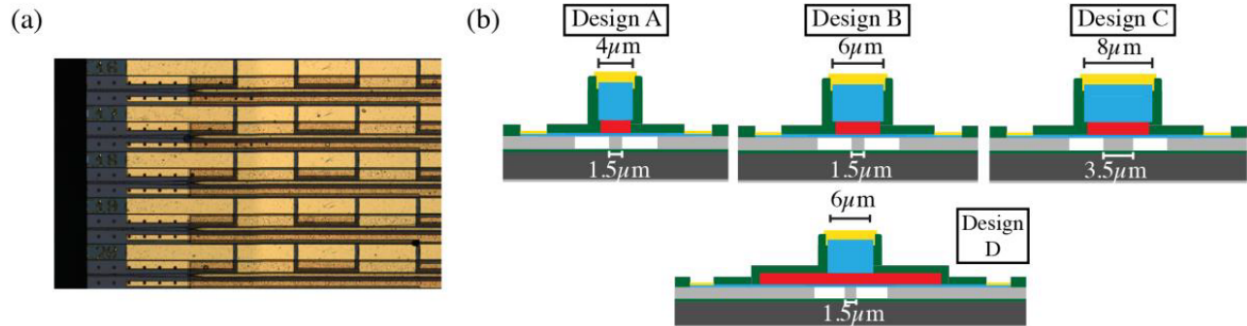


Figure 10. (a) Optical microscope image of DFB QCLs integrated on silicon. (b) Cross-sectional schematic of the active region of four integrated QCL designs.

Figure 11(a) shows a 3D illustration of the SONOI waveguide with an etched surface grating underlying the III-V layers and Fig. 11(b) illustrates the DFB QCL, which consists of a hybrid Si/III-V active region coupled by III-V tapers to passive silicon waveguides on both sides. Output facets are formed by mechanically polishing the passive SONOI waveguides. The 3 mm-long active region is positioned on top of a quarter-wavelength-shifted shallow DFB surface grating that extends throughout the underlying silicon waveguide. The SONOI waveguide is fully etched and 1.5 μm tall. The L-I-V characteristics at 20 °C of each device were measured both before and after removal of the III-V tapers. Figure 11(c) illustrates the DFB QCL after the taper was removed by mechanical polishing, revealing a polished hybrid III-V/Si facet on one end.
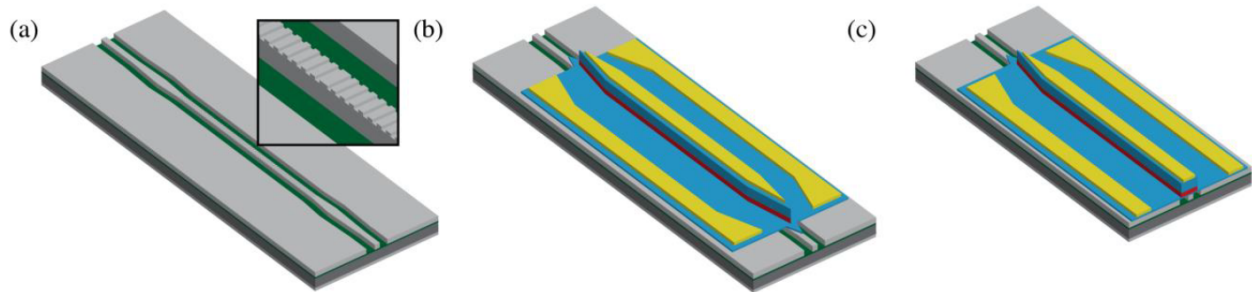


Figure 11. 3-dimensional illustrations of: (a) A silicon waveguide with a shallow etched DFB grating which underlies the bonded III-V QCL material. Inset: a close-up of the quarter-wavelength shift in the center of the DFB grating. (b) A DFB QCL on silicon with polished SONOI waveguide output facets on both ends. (c) A DFB QCL on silicon with a polished hybrid III-V/Si output facet on one end.

Before the silicon waveguide is etched, the grating is patterned onto the silicon with electron beam lithography (EBL) and formed with a $C_4F_8/SF_6/Ar$ inductively coupled plasma (ICP) etch. The grating period ranges from 738 to 778 nm for different devices. A ~31% etched silicon duty cycle and a 28 nm etch depth were measured by atomic force microscope (AFM). Figure 12 shows a simplified fabrication process flow of the DFB QCLs following the grating and silicon waveguide definition.
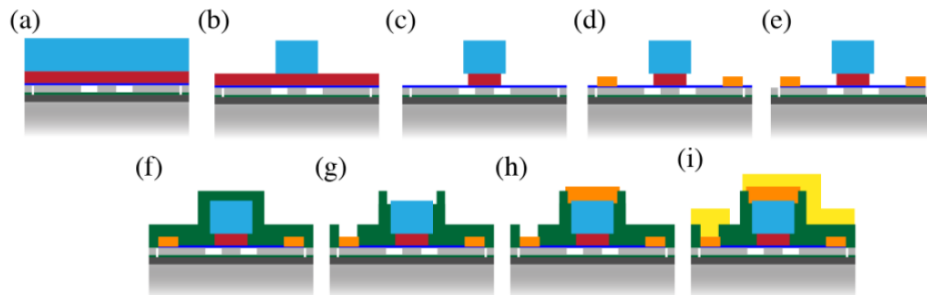


Figure 12. Simplified fabrication process flow: (a) Bond III-V material to silicon waveguides and remove InP substrate by mechanical lapping and selective chemical wet etch. (b) Reactive ion etch (RIE) of upper InP cladding. (c) $H_3PO_4:H_2O_2:H_2O$ wet etch of the QCL active region. (d) Deposit bottom contact metal. (e) RIE etch of bottom InP cladding. (f) Deposit PECVD SiN cladding. (g) Dry etch vias. (h) Deposit top contact metal. (i) Deposit probe metal.

The QCL material was grown by metalorganic chemical vapor deposition (MOCVD) at U. Wisconsin-Madison with 30 active stages and the design was tailored for heterogeneous

integration. In particular, a thin bottom InP contact layer and thick top InP cladding were used to increase optical confinement in the silicon waveguide while preventing overlap with the top metal.

The DFB QCLs were measured at 20 ºC and driven with 250 ns wide pulses at 1 kHz repetition rate. Before removing the tapers, a threshold current density of 0.58 kA/cm$^2$ was measured for a laser of Design D (assuming the current spreads uniformly throughout the 24 μm-wide active region). The maximum output power, however, was only 11 mW for a laser with a differential slope efficiency of only 23 mW/A. These observations would be inconsistent if obtained for a conventional QCL geometry with cleaved facets, since the observed low efficiency implies a high loss, which should greatly increase the threshold current density.

Figure 13 plots the light intensity *vs.* injection current density for lasers of Designs A, B, C, and D, respectively, after removal of the tapers at the laser outputs. In all cases, the threshold current densities increased only slightly (by 7–26%) while the differential efficiencies improved dramatically (by factors of 14–51). Apart from one anomalous device of Design A, the slope efficiencies following removal of the tapers ranged from 161 mW/A (for a laser of Design C) to 541 mW/A (for a laser of Design D). The maximum measured output power was 211 mW (not yet saturated) for a laser of Design D, as seen in Fig. 13. The threshold current densities ranged from 0.71 to 1.36 kA/cm$^2$ for Designs A, B, and D, while the thresholds for devices with Design C were somewhat higher (1.44–1.83 kA/cm$^2$).
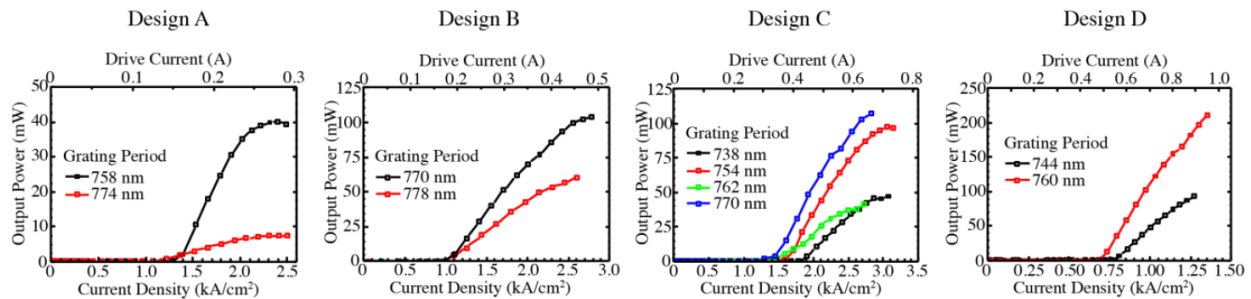


Figure 13. Light intensity *vs.* drive current of integrated DFB QCLs with various active region designs and DFB grating periods.

The low threshold current densities, both before and after the tapers were polished off, indicates that taper limited the collection efficiency outside of the DFB cavity rather than to increase the loss within the primary laser cavity. The slight increase in threshold current after removal of the taper suggests that the reflectivity from the taper is higher than that of the polished (but uncoated) hybrid Si/III-V facet, whereas a large increase in the slope efficiency after the polishing indicates that the transmission through the taper is very low. This is consistent with our conclusions drawn in [13].

Figure 14 shows the spectral measurements for lasers, acquired at 20 °C with a Digikrom 0.5 m monochromator with 1.5 nm resolution. In all cases, a primary lasing peak at a wavelength ranging from 4.62-4.86 μm tracks the central Bragg frequency of the particular DFB grating, although many of the lasers emit in multiple modes. The weaker spectral features likely result from Fabry-Perot resonances corresponding to reflections between the polished hybrid Si/III-V facet and the remaining III-V taper. Inconsistencies of these modes from device to device may be attributed to variations in the taper fabrication associated with non-uniform undercut at the taper tip across the chip after wet etching the active region.
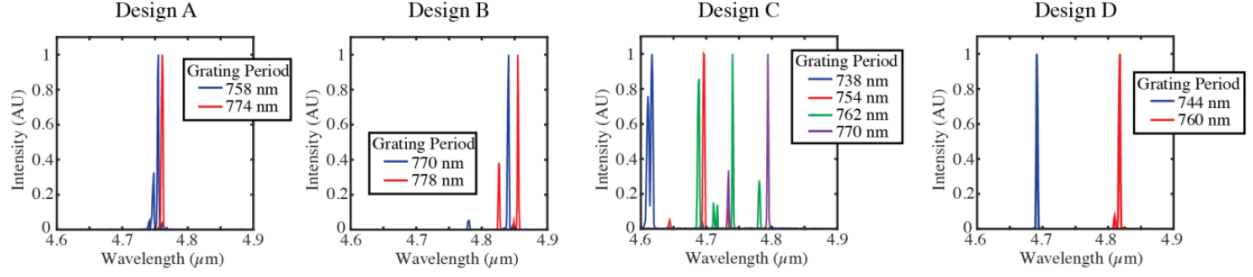
Figure 14. Normalized optical emission spectra of integrated DFB QCLs with various active region designs and DFB grating periods.

Figure 15(a) shows the light output *vs.* drive current for a laser of Design B with grating period 770 nm, measured at a range of temperatures from 10 °C to 100 °C. The extracted characteristic temperatures are $T_0 = 199$ K for threshold and $T_1 = 222$ K for slope efficiency. The maximum operating temperature is significantly higher than that observed for the Fabry-Perot QCLs on silicon [13], which lased in pulsed mode only to 60 °C. The higher $T_0$ and $T_1$ values are consistent with both the significantly lower room temperature threshold current density compared to the Fabry-Perot devices and the relatively low injector sheet-doping density (~0.5 × 10$^{11}$ cm$^{-2}$) [39]. Figure 15(b) shows the emission spectra for the same device over the same range of temperatures. The single primary peak tunes at a rate of 0.25 nm/K, which is consistent with the expected shift of the modal index that governs the DFB mode rather than the shift of the gain peak.
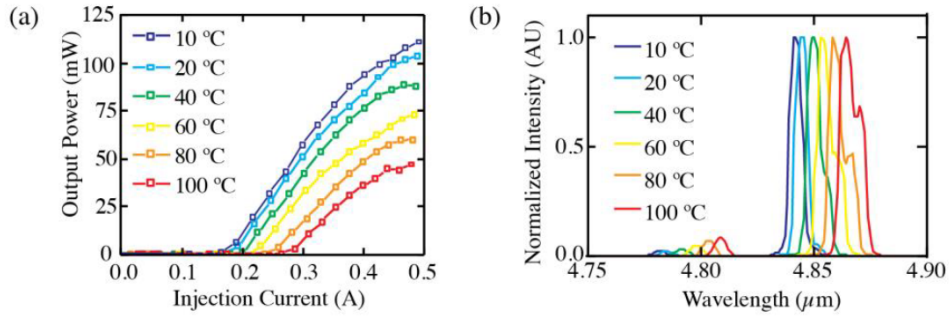


Figure 15. (a) Output power *vs.* injection current of a DFB QCL tested at temperatures from 10 ºC to 100 ºC. (b) Emission spectra of the same DFB QCL tested at temperatures from 10 ºC to 100 ºC.

## 3.3. Integrated spectral beam combining

This section describes the passive wavelength beam combining devices for integration with the different lasers discussed in Section 4. In particular, intra-band, inter-band, and ultra-broadband combiners for dense and course WDM are reviewed.

### 3.3.1. Dense WDM

For the range of wavelengths generated from a single gain material, a dense WDM device will combine each laser output to a single waveguide. AWGs provide the most efficient spectral beam combining for dense spectral spacing. Measurement results for AWGs operating near

0.76-µm, 1.55-µm, and 2.0-µm wavelengths are reviewed and a recently fabricated AWG at 3.6-µm is shown in this sub-section.

Low-loss AWGs are achieved by minimizing loss contributions from waveguide propagation, width transitions, and bend radius transitions. Phase errors in the arrayed waveguides must also be minimized. Additionally, the waveguide array in the AWG must have low side-order excitation. These design aspects become more problematic for shorter wavelengths compared AWGs commonly made in the near-infrared for communication applications. For bulk material, Rayleigh scattering dominates, which is proportional to $\lambda^{-4}$, and for waveguides, interfacial scattering dominates, having a similar wavelength dependence [40,41]. Phase errors arise due to lithography inaccuracies (from mask writing or photoresist exposure), waveguide interfacial roughness, or non-uniformities in the waveguide thickness and in the etch. These fabrication-related limitations have greater effect at reduced wavelengths.
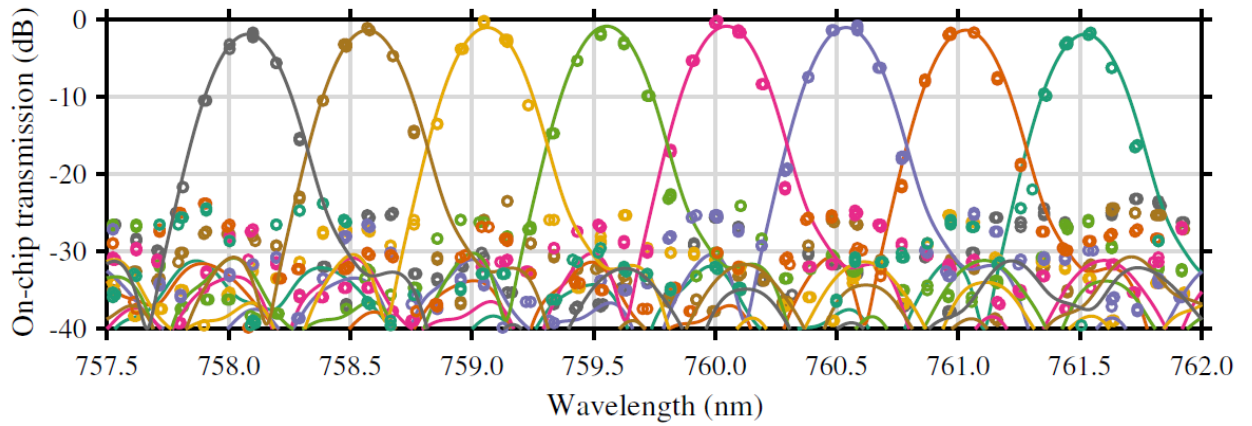


Figure 16. Transmission spectra for the 8 channels of an AWG at 0.76-µm wavelength. Dots show the experimental data and the solid lines are simulations.

To optimize our design tools, an AWG near 0.76-µm wavelength is demonstrated [42] prior to attempting longer wavelength AWGs. The waveguide core is $Si_3N_4$ and cladding is $SiO_2$, consistent with the SONOI platform. A record low loss of <0.5 dB and crosstalk level of −25 dB is reported. The on-chip transmission data and model are plotted in Fig. 16, which show good agreement within the −20-dB peak channel bandwidths. However, the crosstalk level of the model is about 5 dB lower than the data. This is attributed to fabrication variations, such as waveguide thickness and etch non-uniformities, that are not included in the model.
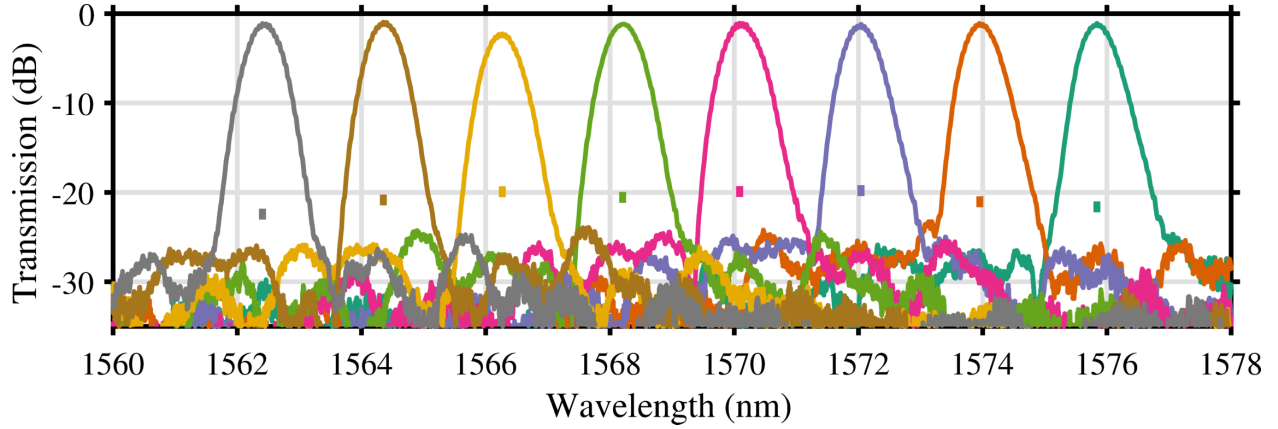
Figure 17. Transmission spectra for 8 channels of an AWG at 1.57-µm wavelength. Dashes show the 3-dB bandwidth cumulative crosstalk.



Figure 18. Transmission spectra for 8 channels of an AWG at 2.0-µm wavelength. Diamonds show the 3-dB bandwidth cumulative crosstalk.

Recently, AWGs near 1.55-µm and 2.0-µm wavelengths have been demonstrated on SOI with eight channels. The 1.55-µm AWG is reported with <1.6 dB of loss and about −29 dB of crosstalk [43], which is shown in Fig. 17. Preliminary measurements of the 2.0-µm AWG reveals a low loss of <1.0 dB and crosstalk at about −28 dB, shown in Fig. 18. Also, a 3.6-µm wavelength AWG has been designed on SOI and the simulated performance is shown in Fig. 19(a) with a micrograph of the device in Fig. 19(b), with loss predicted to be <1.0 dB for all channels.

Figure 19. (a) Micrograph of a ~3.6-µm AWG on SOI. (b) Simulated transmission spectra of the device.

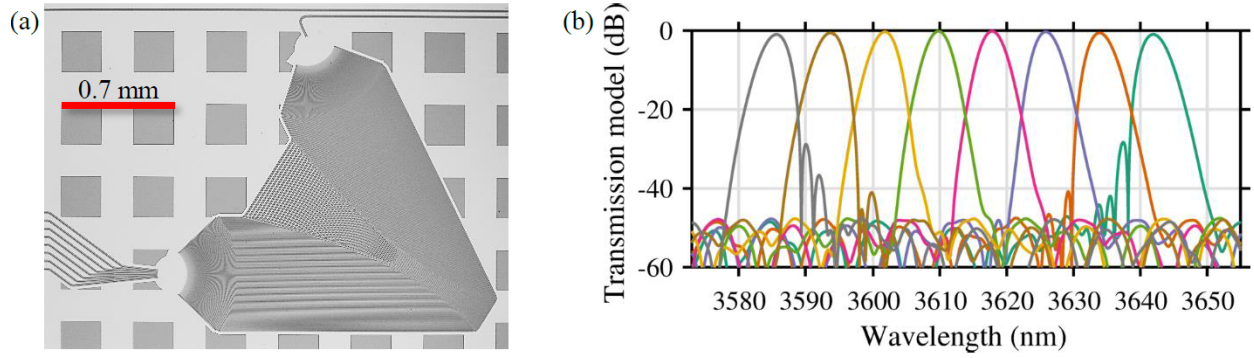Work is in progress to compare the performance of these AWG demonstrations on SOI to similar designs on SONOI. This will indicate if loss decreases with SONOI due to the reduced material absorption of $Si_3N_4$ compared to $SiO_2$ or if excess loss arises from the additional material interfaces. An AWG design on SONOI waveguides for operation at ~4.7-µm wavelength is shown in Fig. 20(a) with the simulated transmission spectra in Fig. 20(b). The loss will likely be dominated by the SONOI propagation loss. Assuming a similar loss to the SOI waveguides at 3.6-µm, this SONOI AWG will also have losses in the range of 0.2–1.2 dB.



Figure 20. (a) Design of a ~4.7-µm AWG on SONOI. (b) Simulated transmission spectra of the device.

### 3.3.2. Course WDM

Inter-band combiners are either realized with adiabatic couplers or AWGs. The adiabatic coupler serves as a wavelength combiner with two inputs and one output, operating over spectral ranges spanning multiple octaves. These duplexers can achieve very low loss, only limited by the waveguide propagation loss (<0.05 dB). AWGs can combine more spectral channels; however, the loss is higher (~1.0 dB) and the bandwidth is narrower.

Figure 21. (a) Schematic top-view of the ultra-broadband combiner, showing the two ports: cross and bar. (b) Top-view micrograph of demonstrated ultra-broadband combiner. (c) Simulation of device performance over 4 octaves and (d,e) measured transmission spectra for devices with short and long coupler lengths, respectively.

The final combiner stage must be ultra-broadband, guiding and combining wavelengths that span more than four octaves to converge each laser output into a single waveguide. For the applications mentioned in t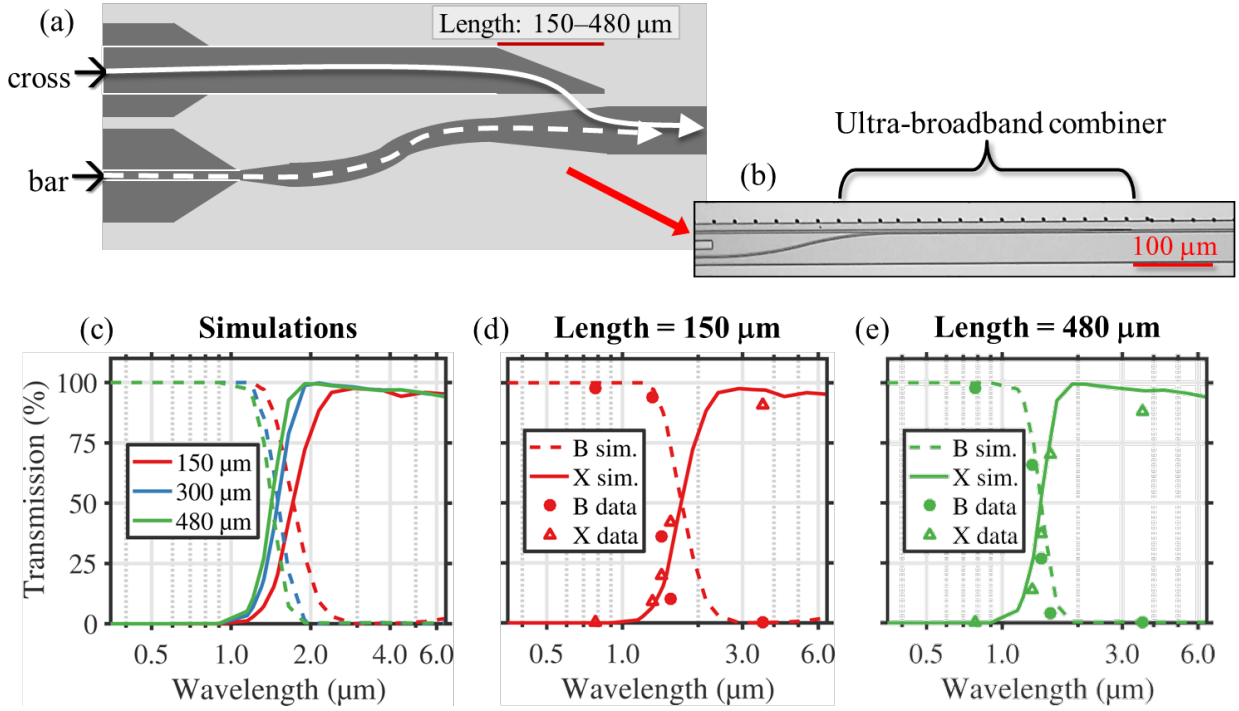he Introduction section, the efficiency of fundamental mode excitation at each wavelength is important because this determines the output beam quality and affects the brightness (B) of the multi-spectral laser. A modified adiabatic coupler has been demonstrated to meet these specifications [8]. This device is schematized in Fig. 21(a) with a micrograph in Fig. 21(b). One input to this combiner supports the short wavelengths and the other the long wavelengths. Figure 21(c) shows the simulated transmission spectra for three different coupler lengths and Figs. 21(d,e) show measurements for the shortest and longest lengths. A narrow spectral region near 1.55-µm exhibits decreased transmission with a maximum loss of 3.0 dB. Less than 0.5-dB loss is found between 0.35-µm to 1.3-µm for one input and 1.9-µm to 6.5-µm light for the other. The center of the low-transmission region can be tuned by changing the length of the coupler, which is independent of the operating bandwidth. The key aspect is that simulated and measured device transmission is from the input fundamental mode to the output fundamental mode for each wavelength. This ensures a near-Gaussian output excitation for low $M^2$ and high brightness.

## 4. Design and feasibility studies of complete multispectral sources

Here we will describe the design of a fully integrated photonic circuit that combines the previously discussed and demonstrated devices into a multispectral source. With added simulations, projections are made for expected device performance in terms of spectral bandwidth and total output power. The first sub-section describes the more conservative 3-band, 10-W device and the second sub-section describes the long-term goal of a 6-band, 100-W architecture.

### 4.1. NIR, SWIR, and MWIR multispectral source: 10-W architecture

At the beginning of this work, the 3-band multi-spectral source was projected to demonstrate a total output power of 10 W. Now that optical sources have been demonstrated at the NIR, SWIR, and MWIR, we can more accurately estimate the total feasible output power of this 3-band device. From the demonstrations discussed in Section 3, we have simulated how much power can be achieved for 3-mm long lasers after improving thermal dissipation by packaging with aluminum nitride (AlN) submounts. The results are summarized in Table 1. A total output power of 19.4 W is estimated for a PIC with 32 channels per band. The simulated beam quality shows $M^2 < 1.7$. Higher power can potentially be achieved by integrating more channels and/or amplifiers.

Table 1. Output power projection for 3-band, 10-W architecture.

| Center wavelength (um) | Single emitter output power (mW) | Beam combining channels | Passive loss, average (dB) | Output power (W) |
|---|---|---|---|---|
| 1.5 | 140 | 32 | 1.5 | 3.2 |
| 2.0 | 58 | 32 | 1.0 | 1.5 |
| 4.8 | 650 | 32 | 1.5 | 14.7 |
| | | | | Sum = 19.4 W |

### 4.2. UV, VIS, NIR, SWIR, MWIR, and LWIR multispectral source: 100-W architecture

The 6-band multispectral source expands on the same platform as the 3-band source. Lasers in three additional wavelength bands (ultraviolet, visible, and long-wave infrared) are added while multiple sources are incorporated in the NIR and MWIR bands. A total of 9 laser sources are integrated. The results are summarized in Table 2 with total estimated output power of 81.6 W. For the spectral bands that have not yet been demonstrated on Si, the output power estimations are extracted from recent demonstrations on native substrates, aside from the 10 μm wavelength band lasers, which we anticipate to achieve performance similar to the 4.8 μm QCLs on silicon.

We expect to achieve a total of over 100-W by improving the output power of all wavelength bands as designs are perfected. Developments in taper transition efficiency, thermal dissipation, current injection efficiency, and packaging will provide marked improvements. In particular, lasers at 1.1-μm, 2.0-μm, 4.8-μm, and 10.0-μm wavelengths are expected to show drastic improvements and realize the higher powers that are demonstrated on their native substrates.

Table 2. Output power projection for 6-band, 100-W architecture.

| Center wavelength (um) | Single emitter output power (mW) | Beam combining channels | Passive loss, average (dB) | Output power (W) |
|---|---|---|---|---|
| 0.4 | 1000 | 32 | 1.5 | 22.7 |
| 0.8 | 250 | 32 | 1.0 | 6.4 |
| 1.1 | 33 | 32 | 1.0 | 0.8 |
| 1.3 | 533 | 32 | 1.5 | 12.1 |
| 1.6 | 140 | 32 | 1.5 | 3.2 |
| 2.0 | 58 | 32 | 1.0 | 1.5 |
| 3.6 | 200 | 32 | 1.0 | 5.1 |
| 4.8 | 650 | 32 | 1.5 | 14.7 |
| 10.0 | 650 | 33 | 1.5 | 15.2 |
| | | | | Sum = 81.6 W |

## 5. Conclusions and recommendations

Each element of the high-brightness multi-spectral laser on silicon has been demonstrated and a path towards complete integration is feasible. High powered lasers spanning the near-infrared to the mid-infrared are integrated on silicon. Low-loss beam combining elements are realized at corresponding wavelengths to the optical sources, paving the way for full-system integration. Remaining challenges for this multi-spectral PIC are to improve laser wall-plug efficiencies and to develop a fabrication process for simultaneous integration of InP with other gain materials.

This technology is important to enable fully-integrated multi-spectral lasers for highly attuned gas sensors, infrared counter-measures, ultra-broadband WDM optical communications, and industrial processing. Fabrication of this device is scalable and would drastically reduce the cost compared to technologies with similar performance.

Projections for the 3-band multispectral source show that 19.4 W is achievable with lasers from three different gain materials, which is higher than the previous estimate of 10 W. By integrating up to nine different gain materials on a single chip, a multispectral source covering the UV to the LWIR (6-bands) is shown to achieve 82W with current technology. Although this is lower the original estimate of 100 W, further improvements to the laser designs are expected to improve the output power of the 6-band device, possibly exceeding 100 W.

# 6. References

[1] Siegman, A., "Analysis of laser beam quality degradation caused by quartic phase aberrations," Appl. Opt. **32**(30), 5893–5901 (1993).

[2] Paschotta, R., "Beam quality deterioration of lasers caused by intracavity beam distortions," Opt. Express **14**(13), 6069–6074 (2006).

[3] Fan, T. Y., "Laser beam combining for high-power, high-radiance sources," IEEE J. Sel. Topics Quantum Electron. **11**(3), 567–577 (2005).

[4] Fang, A. W., Park, H., Cohen, O., Jones, R., Paniccia, M. J., and Bowers, J. E., "Electrically pumped hybrid AlGaInAs-silicon evanescent laser," Opt. Express **14**(20), 9203–9210 (2006).

[5] Liang, D. and Bowers, J. E., "Recent progress in lasers on silicon," Nat. Phot. **4**(8), 511–517 (2010).

[6] Chang, H.-H., Kuo, Y.-h., Jones, R., Barkai, A., and Bowers, J. E., "Integrated hybrid silicon triplexer," Opt. Express **18**(23), 23891–23899 (2010).

[7] Zhang, C., Zhang, S., Peters, J. D., and Bowers, J. E., "8×8×40 Gbps fully integrated silicon photonic network on chip," Optica **3**(7), 785–786 (2016).

[8] Stanton, E. J., Heck, M. J. R., Bovington, J., Spott, A., and Bowers, J. E., "Multi-octave spectral beam combiner on ultra-broadband photonic integrated circuit platform," Opt. Express **23**(9), 11272–11283 (2015).

[9] Davenport, M. L., Skendžić, S., Volet, N., Hulme, J. C., Heck, M. J., and Bowers, J. E., "Heterogeneous Silicon/III-V Semiconductor Optical Amplifiers," IEEE J. Sel. Topics Quantum Electron. **22**(6), 78–88 (2016).

[10] Chang, H.-H., Fang, A. W., Sysak, M. N., Park, H., Jones, R., Cohen, O., Raday, O., Paniccia, M. J., and Bowers, J. E., "1310nm silicon evanescent laser," Opt. Express **15**(18), 11466–11471 (2007).

[11] Spott, A., Davenport, M., Peters, J., Bovington, J., Heck, M. J., Stanton, E. J., Vurgaftman, I., Meyer, J., and Bowers, J., "Heterogeneously integrated 2.0 μm cw hybrid silicon lasers at room temperature," Opt. Lett. **40**(7), 1480–1483 (2015).

[12] Spott, A., Peters, J., Davenport, M. L., Stanton, E. J., Merritt, C. D., Bewley, W. W., Vurgaftman, I., Kim, C. S., Meyer, J. R., Kirch, J., et al., "Quantum cascade laser on silicon," Optica **3**(5), 545–551 (2016).

[13] Liang, D., Fang, A. W., Park, H., Reynolds, T. E., Warner, K., Oakley, D. C., and Bowers, J. E., "Low-Temperature, Strong SiO2-SiO2 Covalent Wafer Bonding for III-V Compound Semiconductors-to-Silicon Photonic Integrated Circuits," J. of Electron. Mater. **37**(10), 1552–1559 (2008).

[14] Liang, D., Chapman, D. C., Li, Y., Oakley, D. C., Napoleone, T., Juodawlkis, P. W., Brubaker, C., Mann, C., Bar, H., Raday, O., et al., "Uniformity study of wafer-scale InP-to-silicon hybrid integration," Appl. Phys. A Mater. Sci. Process. **103**(1), 213–218 (2011).

[15] Volet, N., Spott, A., Stanton, E. J., Davenport, M. L., Chang, L., Peters, J. D., Briles, T. C., Vurgaftman, I., Meyer, J. R., and Bowers, J. E., "Semiconductor optical amplifier at 2.0-μm wavelength on silicon," Laser Photon. Rev., 1600165 (2017).

[16] Spott, A., Peters, J., Davenport, M. L., Stanton, E. J., Zhang, C., Merritt, C. D., Bewley, W. W., Vurgaftman, I., Kim, C. S., Meyer, J. R., Kirch, J., Mawst, L. J., Botez, D., and Bowers, J. E., "Heterogeneously Integrated Distributed Feedback Quantum Cascade Lasers on Silicon," Photonics **3**(2), 35 (2016).

[17] Piels, M., Bauters, J. F., Davenport, M. L., Heck, M. J., and Bowers, J. E., "Low-loss silicon nitride AWG de-multiplexer heterogeneously integrated with hybrid III-V/silicon photodetectors," J. Lightw. Technol. **32**(4), 817–823 (2014).

[18] Bovington, J., Heck, M., and Bowers, J., "Heterogeneous lasers and coupling to $Si_3N_4$ near 1060 nm," Opt. Lett. **39**(20), 6017–6020 (2014).

[19] Soref, R. A., Emelett, S. J., and Buchwald, W. R., "Silicon waveguided components for the long-wave infrared region," J. Opt. A: Pure Appl. Opt. **8**(10), 840–846 (2006).

[20] Soref, R., "Mid-infrared photonics in silicon and germanium," Nat. Photon. **4**(8), 495–497 (2010).

[21] Li, W., Anantha, P., Bao, S., Lee, K. H., Guo, X., Hu, T., Zhang, L., Wang, H., Soref, R., and Tan, C. S., "Germanium-on-silicon nitride waveguides for mid-infrared integrated photonics," Appl. Phys. Lett. **109**(24), 241101 (2016).

[22] Ramirez, J. M., Vakarin, V., Gilles, C., Frigerio, J., Ballabio, A., Chaisakul, P., Le Roux, X., Alonso-Ramos, C., Maisons, G., Vivien, L., et al., "Low-loss Ge-rich Si0:2Ge0:8 waveguides for mid-infrared photonics," Opt. Lett. **42**(1), 105–108 (2017).

[23] Zhang, C., Srinivasan, S., Tang, Y., Heck, M. J., Davenport, M. L., and Bowers, J. E., "Low threshold and high speed short cavity distributed feedback hybrid silicon lasers," Opt. Express **22**(9), 10202–10209 (2014).

[24] Koch, B. R., Norberg, E. J., Kim, B., Hutchinson, J., Shin, J.-H., Fish, G., and Fang, A., "Integrated silicon photonic laser sources for telecom and datacom," in [National Fiber Optic Engineers Conference], Paper PDP5C-8, OSA (2013).

[25] Liu, H.-F., "Integrated silicon photonics links for high bandwidth data transportation," in [Optical Fiber Communication Conference], Paper Th1D.1, OSA (2014).

[26] Casey Jr., H. C. and Carter, P. L., "Variation of intervalence band absorption with hole concentration in p-type InP," Appl. Phys. Lett. **44**(1), 82–83 (1984).

[27] Volet, N. and Kapon, E., "Turn-on delay and Auger recombination in long-wavelength vertical-cavity surface-emitting lasers," Appl. Phys. Lett. **97**(13), 131102 (2010).

[28] Glassbrenner, C. and Slack, G. A., "Thermal conductivity of silicon and germanium from 3°K to the melting point," Phys. Rev. **134**(4A), A1058 (1964).

[29] Bristow, A. D., Rotenberg, N., and van Driel, H. M., "Two-photon absorption and Kerr coe_cients of silicon for 850–2200 nm," Appl. Phys. Lett. **90**(19), 191104 (2007).

[30] Foster, M. A., Turner, A. C., Sharping, J. E., Schmidt, B. S., Lipson, M., and Gaeta, A. L., "Broad-band optical parametric gain on a silicon photonic chip," Nature **441**(7096), 960–963 (2006).

[31] Zlatanovic, S., Park, J. S., Moro, S., Boggio, J. M. C., Divliansky, I. B., Alic, N., Mookherjea, S., and Radic, S., "Mid-infrared wavelength conversion in silicon waveguides using ultracompact telecom-band-derived pump source," Nat. Photon. **4**(8), 561–564 (2010).

[32] Del'Haye, P., Herr, T., Gavartin, E., Gorodetsky, M., Holzwarth, R., and Kippenberg, T. J., "Octave spanning tunable frequency comb from a microresonator," Phys. Rev. Lett. **107**(6), 063901 (2011).

[33] Chang, L., Li, Y., Volet, N., Wang, L., Peters, J., and Bowers, J. E., "Thin _l um wavelength converters for photonic integrated circuits," Optica **3**(5), 531–535 (2016).

[34] Rothman, L. S., Gordon, I. E., Babikov, Y., Barbe, A., Benner, D. C., Bernath, P. F., Birk, M., Bizzocchi, L., Boudon, V., Brown, L. R., Campargue, A., Chance, K., Cohen, E. A., Coudert, L. H., Devi, V. M., Drouin, B. J., Fayt, A., Flaud, J.-M., Gamache, R. R., Harrison, J. J., Hartmann, J.-M., Hill, C., Hodges, J. T., Jacquemart, D., Jolly, A., Lamouroux, J., Roy,

R. J. L., Li, G., Long, D. A., Lyulin, O. M., Mackie, C. J., Massie, S. T., Mikhailenko, S., Muller, H. S. P., Naumenko, O. V., Nikitin, A. V., Orphal, J., Perevalov, V., Perrin, A., Polovtseva, E. R., Richard, C., Smith, M. A. H., Starikova, E., Sung, K., Tashkun, S., Tennyson, J., Toon, G. C., Tyuterev, V. G., and Wagner, G., "The HITRAN2012 molecular spectroscopic database," J. Quant. Spectrosc. Radiat. Transfer **130**, 4–50 (2013).

[35] Salisbury, J. W. and D'Aria, D. M., "Emissivity of terrestrial materials in the 3–5 μm atmospheric window," Remote Sens. Environ. **47**(3), 345–361 (1994).

[36] Gu, Y., Zhang, Y., Cao, Y., Zhou, L., Chen, X., Li, H., and Xi, S., "2.4 μm InP-based antimony-free triangular quantum well lasers in continuous-wave operation above room temperature," Appl. Phys. Express **7**(3), 032701 (2014).

[37] Bai, Y., Bandyopadhyay, N., Tsao, S., Slivken, S., and Razeghi, M., "Room temperature quantum cascade lasers with 27% wall plug efficiency," Appl. Phys. Lett. **98**(18), 181102 (2011).

[38] Yao, Y., Hoffman, A. J., and Gmachl, C. F., "Mid-infrared quantum cascade lasers," Nat. Photon. 6(7), 432–439 (2012).

[39] Botez, D., Chang, C.-C. and Mawst, L. J., "Temperature sensitivity of the electro-optical characteristics for mid-infrared ($\lambda = 3$–16 μm)-emitting quantum cascade lasers," J. Phys. D: Appl. Phys. **49**, 043001 (2016).

[40] Bauters, J. F., Heck, M. J., John, D. D., Barton, J. S., Bruinink, C. M., Leinse, A., Heideman, R. G., Blumenthal, D. J., and Bowers, J. E., "Planar waveguides with less than 0.1 dB/m propagation loss fabricated with wafer bonding," Opt. Express **19**(24), 24090–24101 (2011).

[41] Barwicz, T. and Haus, H. A., "Three-dimensional analysis of scattering losses due to sidewall roughness in microphotonic waveguides," J. Lightw. Technol. **23**(9), 2719 (2005).

[42] Stanton, E. J., Spott, A., Davenport, M. L., Volet, N., and Bowers, J. E., "Low-loss arrayed waveguide grating at 760 nm," Opt. Lett. **41**(8), 1785–1788 (2016).

[43] Stanton, E. J., Volet, N., and Bowers, J. E., "Ring resonator with cascaded arrayed waveguide gratings for accurate insertion loss measurement," in [IEEE Photonics Conference (IPC)], Paper MB3.4 (2016).